Journal of composites science

MDPI

Article

Human Skin-Like Composite Materials for Blast Induced Injury Mitigation

Arnab Chanda [1,2,*] and Rebecca Graeter [3]

[1] Department of Bioengineering, University of Pittsburgh, Pittsburgh, PA 15213, USA
[2] Department of Aerospace Engineering and Mechanics, University of Alabama, Tuscaloosa, AL 35401, USA
[3] Department of Chemical Engineering, Mississippi State University, Starkville, MS 39759, USA; rg814@msstate.edu
* Correspondence: arc165@pitt.edu; Tel.: +1-205-887-5642

Received: 8 June 2018; Accepted: 24 July 2018; Published: 1 August 2018

Abstract: Armors and military grade personal protection equipment (PPE) materials to date are bulky and are not designed to effectively mitigate blast impacts. In the current work, a human skin-like castable simulant material was developed and its blast mitigation characteristics (in terms of induced stress reduction at the bone and muscles) were characterized in the presence of composite reinforcements. The reinforcement employed was Kevlar 129 (commonly used in advanced combat helmets), which was embedded within the novel skin simulant material as the matrix and used to cover a representative extremity based human skin, muscle and bone section finite element (FE) model. The composite variations tested were continuous and short-fiber types, lay-ups (0/0, 90/0, and 45/45 orientations) and different fiber volume fractions. From the analyses, the 0/0 continuous fiber lay-up with a fiber volume fraction close to 0.1 (or 10%) was found to reduce the blast-induced dynamic stresses at the bone and muscle sections by 78% and 70% respectively. These findings indicate that this novel skin simulant material with Kevlar 129 reinforcement, with further experimental testing, may present future opportunities in blast resistant armor padding designing.

Keywords: blast; composite; skin; traumatic brain injury (TBI); finite element

1. Introduction

Blasts have been a major cause of traumatic injuries among soldiers involved in armed combats in politically disturbed areas such as Iraq and Afghanistan [1]. Besides mild traumatic brain injury (TBI), severe whole-body injuries are often reported, which could be mainly attributed to poorly designed armors and military grade personal protection equipment (PPE). To date, realistic experimental modeling has been a challenge due to difficulty in simulating blasts and ethical issues associated with animal and human testing. This has led to extensive computational efforts into investigation of ballistic and blast-induced mitigation [2,3] effects of armors, specifically helmet materials including composite based paddings. An axisymmetric numerical model of the head and helmet was developed by Khalil et al. [4] to study the helmet's load response for a short duration ballistic impact. Several studies were conducted by Hoof et al. [5,6] on the impact of ballistic loading on the personnel armor system for ground troops (PASGT) helmet, which indicated that ballistic impacts mainly caused localized effects at the impact area, with minimal effects on the rest of the helmet. Impact of a high velocity ballistic studied by Baumgartner et al. [7] revealed a risk of skull fracture due to helmet back force deformation (BFD). Aare et al. [8] investigated how helmet shell stiffness and impact direction influences head injury, and found that to avoid injury, the shell deflection should not be more than the initial distance between the head and the helmet. Lee et al. [9] studied the effect of varying helmet cushioning on ballistic head impacts. It was concluded that the helmets with all types of cushions protect well

against small projectiles, but poorly for large ballistics. Tan et al. [10] studied the impact performance of advanced combat helmet (ACH) using finite element (FE) analysis, which indicated the superior characteristics of low hardness foams for ballistic impact mitigation. Li et al. [11] also studied the effect of ballistic impacts on ACH, and found that large, medium, and small values of BFD occurred due to frontal, crown and lateral impacts respectively. Also, BFD was found to decrease in correspondence with a decrease in oblique impact angle. Additionally, the simulations indicated that the BFD was inversely related to the helmet size for the same impact velocity. Recently, Rodriguez-Millan et al. [12] studied the effect of standard ballistic impacts on a combat helmet, and based on the experiments, developed a complex and high fidelity numerical model of the helmet. This numerical model was used to study the ballistic limit of the helmet, which correlated well with the experimental results. The study concluded that the computational model was biofidelic and appropriate for modeling different ballistics tests on the combat helmet.

With respect to the study of blast induced impacts, most injury incidences have occurred due to shockwave induced overstressing of the cranium [13]. Another major localized overpressure causing effect has been identified to be the underwash effect, in which the incoming shockwave interacts with the amount of wave reflected from helmets, causing pressure amplification at different head locations. Ganpule et al. [14] developed a 2D FE model to study the interaction effect of a head and a frontal blast shockwave in both the presence and absence of a protective helmet. Amplified underwash pressures were recorded, which was attributed to the helmet geometry, curvature and gap between the head and the helmet. Moss et al. [15] observed the significantly reduced effect of underwash effects in the presence of helmet foam pads, however with a consequent increase in the couple moments between the head and the helmet causing localized pressure buildups. Zhang et al. [16] also modeled the effect of frontal blast loading on the head in presence of a helmet with padding. The results from the study indicated reduced pressure transmissions to the brain, however accompanied with a high pressure underwash effect at the back of the head. Nyein et al. [17] modeled the stress reducing effects of a military grade helmet and face shield in frontal blast simulations. Significant stress reductions were observed at the brain, however the effect of blast direction and underwash effect were not modeled. To further investigate the underwash effect, Moghaddam et al. [18–21] developed a detailed FE model of the head and tissues, and studied the biomechanical responses of the tissues due to blast waves travelling from different directions. Three models were studied: The unprotected head, semi-protected head (with helmet), and fully protected head with helmet and face shield. From the analyses, the pressure increase due to the underwash effect was found to significantly vary with the incident blast wave direction. Also, the intracranial pressure (ICP) was found to increase due to the underwash effect beyond the peak ICP recorded for a helmet protected head subjected to blast. Rodriguez-Millan et al. [22] recently developed a detailed computational model of the human head including the various sections of the brain (i.e., white matter, grey matter, ventricular system, cerebellum, and brain stem), to study the contribution of advanced combat helmet parts in blast mitigation. The separate helmet parts modeled were the helmet structure, visor, and mandible guard. The results indicated that the individual helmet components were not effective enough in mitigating blast damage, and all the helmet components together were able to reduce blast damage up to five times. Grujicic et al. [23] studied the blast mitigation efficiency of a combat helmet with elastomer based polyuria as the padding material for a numerically modeled head, and found it to perform better than the conventional ethylene-vinyl-acetate (EVA) foam. Grujicic et al. [24] also investigated the energy dissipation and shockwave attenuation capabilities of granular materials. Recently, Jenson et al. [25,26] developed a simple FE model to study the effect of blast on a helmet made of nanocomposite based material, and compared its performance with that of the ACH.

Besides the numerical analysis of blast impacts on the head, very few computational studies have considered the effect of blasts on the rest of the human body such as the extremities, described in Chanda et al. [27,28]. Also, a key literature gap also exists in modeling of composite materials for improved blast resistance in parts of the body other than the head. Besides blast impact mitigation,

other requirements of such materials include light weight, tailorability, and flexibility [27]. Based on the recent developments on human tissue simulants [29–32], a novel skin simulant material was developed and recreated within a FE model. Kevlar 129 fibers (typically used in combat helmets) were embedded into the novel skin simulant (as the matrix material) numerically to simulate a two-layer composite covering. This composite covering was used to protect a representative extremity-based skin, muscle and bone section FE model. The blast mitigation effectivity of the two-layer composite covering was evaluated for varying reinforcement types, lay-ups, and fiber volume fractions. Section 2 discusses the material fabrication and testing, and the FE model development. Section 3 will discuss the results, followed by the conclusions in Section 4.

2. Materials and Methods

A representative extremity based computational model of the skin, muscle and bone section was developed, and covered with two layers of a composite material (made of Kevlar 129 embedded within a novel elastomer-based skin simulant matrix material). Figure 1 shows the section of a hand glove, which could possibly be reinforced with the two composite covering layers to protect the underlying skin, muscle and bone sections from blasts. The various dimensions used to model each of the sections are presented in Figure 1. Also, it should be mentioned that a curved model was selected because none of the human body parts are flat, and have a certain amount of curvature everywhere [33]. This curvature has been found to have an effect on blast loading [34]. The following sections discuss the fabrication and testing of the skin simulant material, material characterization, geometrical model, meshing, the loads and boundary conditions used in the FE analyses.

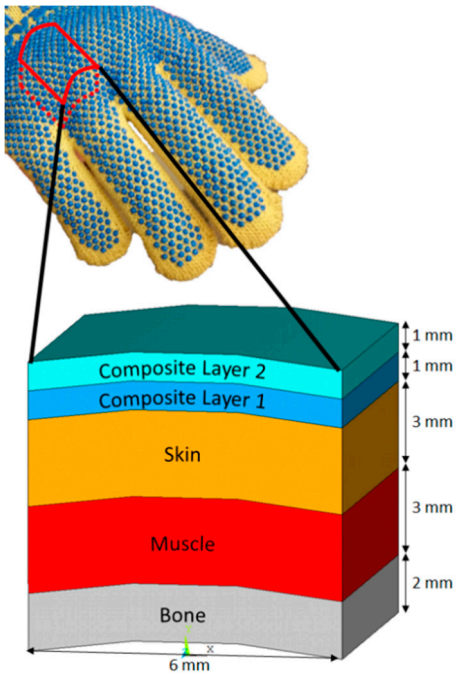

Figure 1. Our computational model of a representative extremity based skin, muscle, and bone section. Also shown are the two layers of protective composite covering.

2.1. Fabrication and Testing of Skin Simulant Material

A two-part soft elastomer material (shore hardness 30 A) from Smooth-On Inc. (Macungie, PA, USA) was mixed in 1:1 weight ratio. 20 test specimens were generated, each of which were clamped onto a uniaxial tensile testing machine (from MTS Corporation, Eden Prairie, MN, USA). Each test specimen had a 35 mm length, 9 mm width and 2.5 mm thickness after clamping (See Figure 2),

and a test rate of 0.4 mm/s was selected for all the tests, based on literature [35]. The average stress versus stretch response obtained from the tensile tests (see Figure 3) were found to lie within the bounds of the human skin mechanical properties [35].

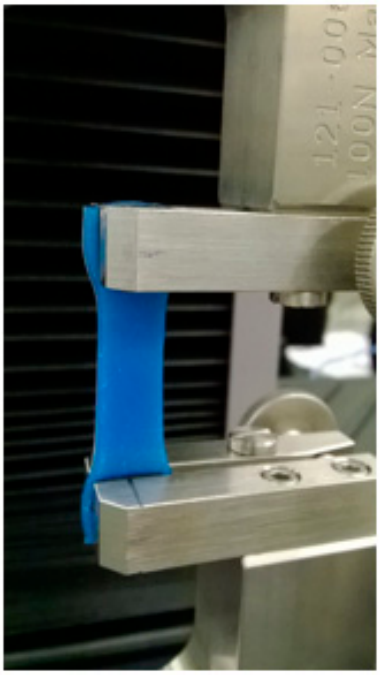

Figure 2. Skin simulant matrix material during a test.

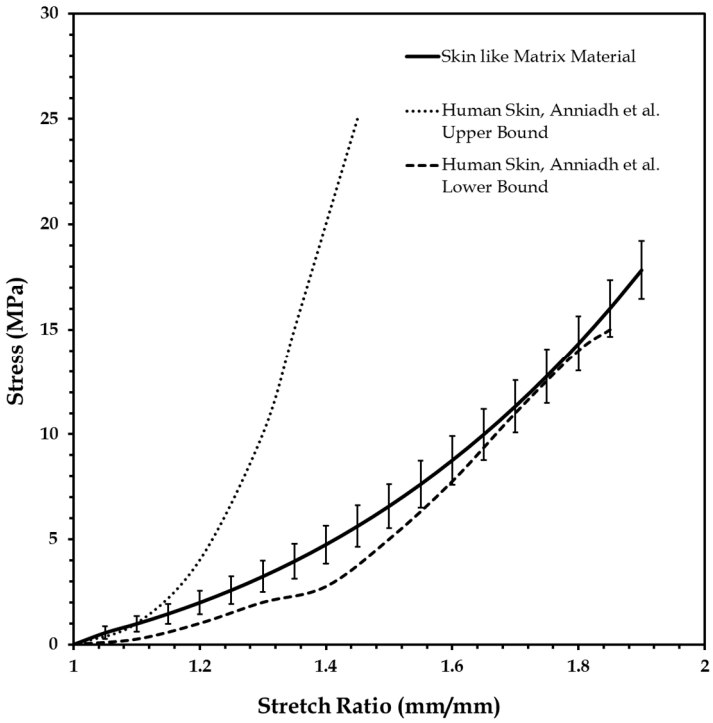

Figure 3. Stress versus stretch response of the skin simulant matrix material, lying within the bounds of the human skin mechanical properties reported in literature [35].

The novel skin simulant material was developed for the matrix material of the composite coverings because it is as flexible as the human skin, and thus can stretch with the movement of the body location where the reinforced armor is placed, without any discomfort [36]. Also, this elastomer material can be casted in any shape or size. Thereby, depending on the shape and curvature of the body location, subject-specific armor designs can be made. Additionally, the skin simulant material is light weight with an estimated density of 0.00091 g/mm^3. The following section discusses the characterization methodology of this skin simulant matrix material, which allowed us to use it further in the computational study.

2.2. Linear and Non-Linear Material Models Used in Computational Study

Elastomers are soft materials, which have non-linear mechanical behavior under tensile loads [37]. Hyperelastic curve-fit formulations such as the Fung model, Mooney-Rivlin's model, and Yeoh's model are used often to characterize the load response of soft materials [38–41]. Hyperelastic constitutive equations are based on the definition of the material specific strain-energy density functions (symbolically written as ψ) [42–48]. The strain energy density function typically depends on the principal stretches (λ_i, i = 1, 2 and 3) along the Cartesian coordinate axes, or the invariants (I_i, i = 1, 2 and 3) of the Cauchy-green tensor, which are the functions of the principal stretches (see Equation (1)). In the current study, the Yeoh's model was used to characterize the non-linear behavior of the soft matrix material. The Yeoh's strain energy density function is given by Equation (2).

$$I_1 = \sum_{i=1}^{3} \lambda_i^2, I_2 = \sum_{i,j=1}^{3} \lambda_i^2 \lambda_j^2, I_3 = \prod_{i=1}^{3} \lambda_i^2 \tag{1}$$

$$\psi_{\text{Yeoh}} = \sum_{i=1}^{3} C_{i0}(I_1 - 3)i + \frac{K}{2}(J-1)^2 \tag{2}$$

Equation (3) presents the relation between the stress, stretch and the strain energy density function, for a uniaxial mechanical test. Solving simultaneously for Equations (2) and (3), the stress versus stretch relationship is given by Equation (4). The stress versus stretch data obtained for the skin simulant (used as the matrix material) in the previous section was characterized using Equation (4). The various curve fit parameters c_{10}, c_{20} and c_{30} were estimated (Table 1). It should be mentioned here that the strength of blast loading (or strain rates) may significantly affect tissue or tissue simulant properties. This effect has not been considered in the present study, which may change the results to some extent. This should be acknowledged as a limitation of this work.

$$\sigma_1 = \lambda_1 \frac{\partial \psi}{\partial \lambda_1} - \lambda_3 \frac{\partial \psi}{\partial \lambda_3}, \sigma_2 = \sigma_3 = 0 \tag{3}$$

$$\sigma_{\text{Yeoh}} = 2(\lambda^2 - \frac{1}{\lambda})(c_{10} + 2c_{20}(I_1 - 3) + 3c_{30}(I_1 - 3)^2), d_i = \frac{2}{K} \tag{4}$$

The elasticity modulus of Kevlar 129 fiber material [49,50], human skin, muscle, and bone were obtained from recent literature [31,47,48,51–56], and are listed in Table 1. The composite material changes due to varying fiber volume fractions [57] have been modeled within the FE system, using different fiber cross-sections and lengths, and not by modifying the global material property of the composite using the rule of mixtures.

Table 1. Body section, and composite material model parameters used in the numerical study.

Non-Linear Material Property for Skin Simulant Used as Matrix Material				
Yeoh Model Parameters	c_{10} **(MPa)**	c_{20} **(MPa)**	c_{30} **(MPa)**	***d1*, *d2* and *d3***
	0.946	4.948	0.015	0.225
Linear Material Properties for Kevlar 129 Fibers				
Modulus of Elasticity (MPa)			**Poisson's Ratio**	
200,000			0.3	
Material Properties for Body Sections from Literature				
Linear Elastic Parameters	**Modulus of Elasticity (MPa)**		**Poisson's Ratio**	
Skin	5		0.49	
Muscle	100		0.46	
Bone	15,000		0.2	

2.3. Geometrical Model

The human skin comprises of three layers namely the epidermis, dermis and the hypodermis, with an overall thickness of 1 to 4 mm [58]. The muscle layer is widely varying in thickness ranging from almost zero (in areas such as the skull) to 3 cm and above (in thighs and biceps) [59–61]. In our current work, a 2 mm section of the bone was modeled, followed by a 3 mm muscle and 3 mm skin layers. All these layers were modeled in FE software ANSYS APDL (17.1, Ansys, Inc., Canonsburg, PA, USA), using the bottom-up approach, starting with key points, followed by creation of splines, areas and volumes. The slight curvature to the model was given to realistically model a section of the human body, which is typically curved and not flat. Additionally, all the adjacent layers were made to share a common surface, so that loads can transfer from one section to another in the FE analyses.

Computational models of two-layer composite coverings (made of Kevlar 129 fibers, embedded within an elastomer-based skin simulant matrix material) was used to cover the skin, muscle and bone section layers against the blast loading. Figure 4 shows the geometrical models with continuous fiber based composite lay-ups namely 0-0, 90-0, and 45-45 orientations. The models with the 45-45 lay-up orientations (see Figures 4 and 5) were modeled as cubical section unlike the other models which are cuboidal in shape. This was done to simplify the fiber lay-up for the 45-45 orientation and make it symmetric. However, it should be mentioned that this slight difference in the model geometry was assumed to have a minimal effect on the results, due to the type of constraint and load application methodology adopted for the analyses (discussed in the upcoming sections). Also, it should be added that the composite configurations tested in this work are just the fundamental composite configurations tested numerically for better understanding of the mechanical behavior of the proposed novel composite layers under blast loading. The experimental composite configurations provided by aramid manufacturers may be widely different, which will be tested in future studies using shock tubes.

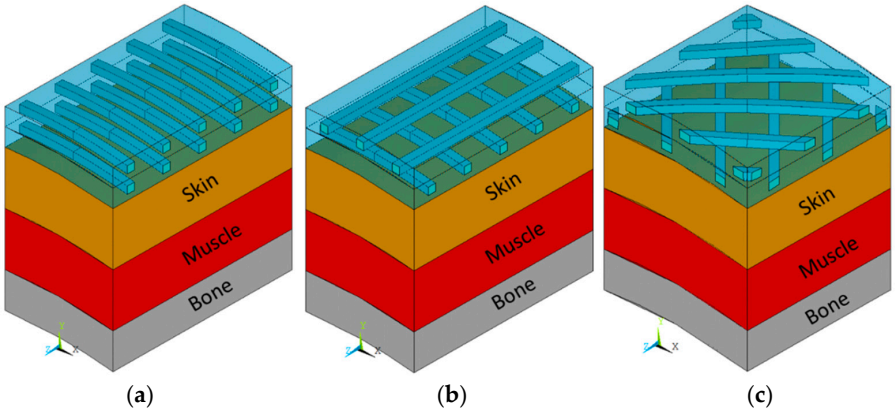

Figure 4. Computational models with continuous fiber-based composite covering layers, namely: (**a**) 0-0 (cuboidal), (**b**) 90-0 (cuboidal), and (**c**) 45-45 (cubical) lay-up orientations.

Short fiber composite materials typically have a length as 100 times the fiber outer diameter [57]. Since most of the fibers are thinner than the human, short fibers may look like powder to the naked eye. Also, it is very difficult to align short fibers in a certain orientation, but may be achievable with advanced manufacturing techniques [62]. In the current work, for simplification of the geometry and to also investigate orientation effects, short fiber-based composite covering layers with 0-0, 90-0, 45-45 lay-ups were modeled (see Figure 5).

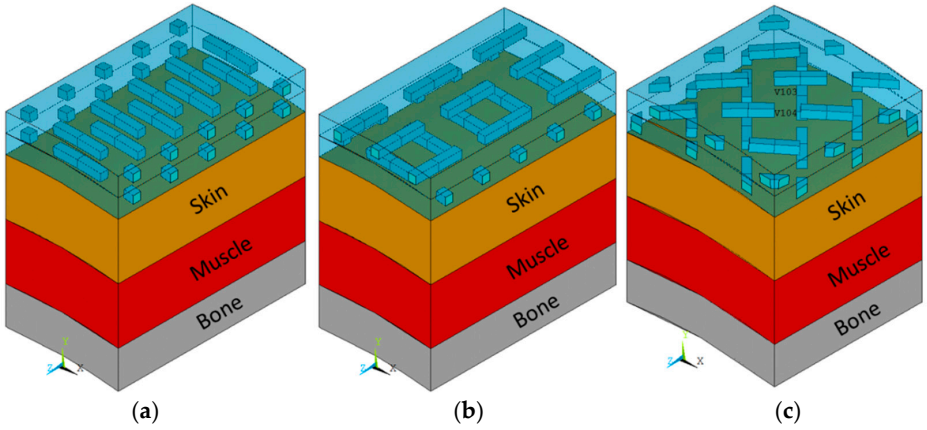

Figure 5. Computational models with short fiber-based composite covering layers, namely: (**a**) 0-0 (cuboidal), (**b**) 90-0 (cuboidal), and (**c**) 45-45 (cubical) lay-up orientations.

In both the composite covering layers, the matrix was modeled first, followed by the fibers (which are also curved). The fibers were perfectly bonded with the matrix using the overlap operation in ANSYS APDL. A square cross-section was chosen for the fibers over a circular cross-section, because it helps in better control of the number of mesh elements, and the mesh size [56] during the FE analyses. Also, the spacing between the adjacent fibers were kept same throughout.

2.4. Finite Element Modeling

In the current work, the fibers were meshed first, followed by the composite skin simulant matrix material, skin, muscle, and the bone sections [56,63–65]. Figure 6 captures the meshes of the various sections from a 90-0 continuous lay-up case. The integrated mesh is also shown in Figure 6.

The fibers were meshed using mapped brick mesh and with sizing controls such that for the cross-section, all the four edges have just one element division [56]. This smart meshing technique

helped us to obtain a reasonable number of mesh elements for the fibers. The two composite skin simulant matrix layers were meshed next with a free tetrahedral type mesh. The skin, muscle, and the bone sections were meshed using sweep mesh, starting at the common surface shared between the second composite layer (meshed with tetrahedral elements) and the skin layer. A higher order 3D 20-node Solid 186-type quadratic tetrahedral element was chosen for the volume meshes. This robust element type was selected as it is used widely in the industry and supports large deflection, creep, large strains, hyperelasticity, plasticity, and stress stiffening [66].

In the computational model in Figure 6, X and Z axes were selected along and orthogonal to the direction of fibers respectively, and Y axis was along the depth of the layers. For each layer, flexible boundary conditions were placed on the four sides, including constraining of translation along the Y axis (to allow the blast load to effectively transmit through the different layers similar to in case of pure bending of rectangular plates [57]). The translation along the X and Z axes were not constrained to allow interaction of the unit cell like computational section model with the adjacent similar sections through shear deformation. The rotations were constrained along all axes, simulating a rigid and high inertia skin-muscle-bone section with well fastened protective composite layers. It should be mentioned here that if the boundary conditions associated with the edges of the studied unit cell were modified (such as if they were deformable in all directions), the stress distribution results may significantly change as observed previously by Chanda et al. [34]. Therefore, the results from this analysis should not be extrapolated beyond the modeled boundary conditions. The bottom of the bone section (which was modeled as a small representative part of the entire bone underneath) was constrained in all degrees of freedom to simulate its strong attachment with underlying bone tissue. Flexible contact pairs were defined to the capture the attachments of the different layers. For the contact pair, a normal penalty stiffness of 1, penetration tolerance of 0.1, and a contact algorithm based on augmented Lagrangian method was selected. The contact surfaces were considered as fully bonded with null initial penetration and surface offset. An automatic contact adjustment for gap closure and penetration reduction was adopted for the analyses.

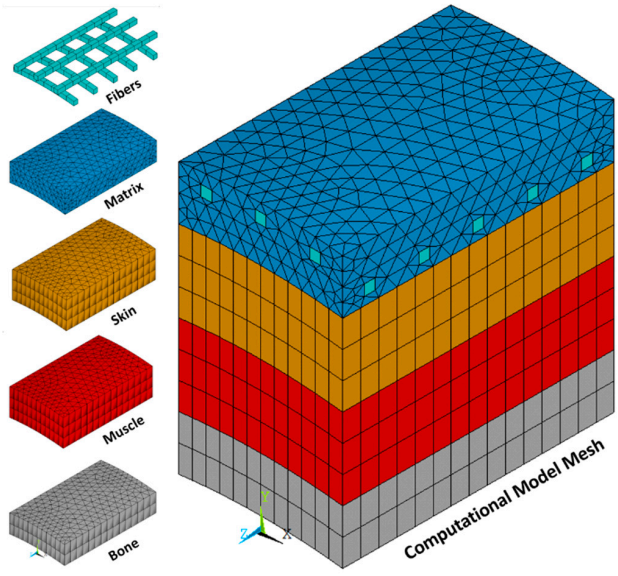

Figure 6. Meshes of the various layers of the bone, muscle and skin section, and the composite covering layers, of the computational model.

A time varying Friedlander type blast loading was applied on the top surface of the composite covering layer with the load steps listed in Table 2, using a dynamic analysis in ANSYS APDL [34]. The induced von Mises stresses in different layers were quantified.

Table 2. Various load steps simulating a time varying Friedlander type blast loading, used in the computational model.

Load Step	Time (ms)	Pressure (MPa)
1	0 to 0.5	0
2	0.5 to 0.6	0.35
3	0.6 to 1.0	−0.05
4	1.0 to 3.0	0

3. Results and Discussion

In a primary blast impact, bone fracture and muscle rupture are the most commonly observed phenomena, mainly during the peak blast pressure [67–69]. Thereby, the stresses at the bone and muscle sections were estimated for the unprotected bone, muscle and skin model in the following section. The blast-induced bone and muscle stresses due to the composite protection covering with varying fiber length (continuous and short fiber) and lay-ups (0-0, 90-0, and 45-45 orientations) have also quantified.

3.1. Blast Stresses in Unprotected Bone, Muscle and Skin Section Model

Figure 7a shows the mesh of the unprotected cubical model. Very high peak stresses were observed at the center of the bone section (Figure 7b). The muscle being a soft tissue, the stresses were observed to have a much more uniform distribution than in the bone section (Figure 7c). Additionally, the peak stress values observed were consistent with the peak stresses observed on the bone and muscle sections due to blast loading in previous work by Chanda et al. [34]. It should be mentioned here that some high stresses were observed at the edges due to the choice of constraints in the FE model (discussed in the previous section).

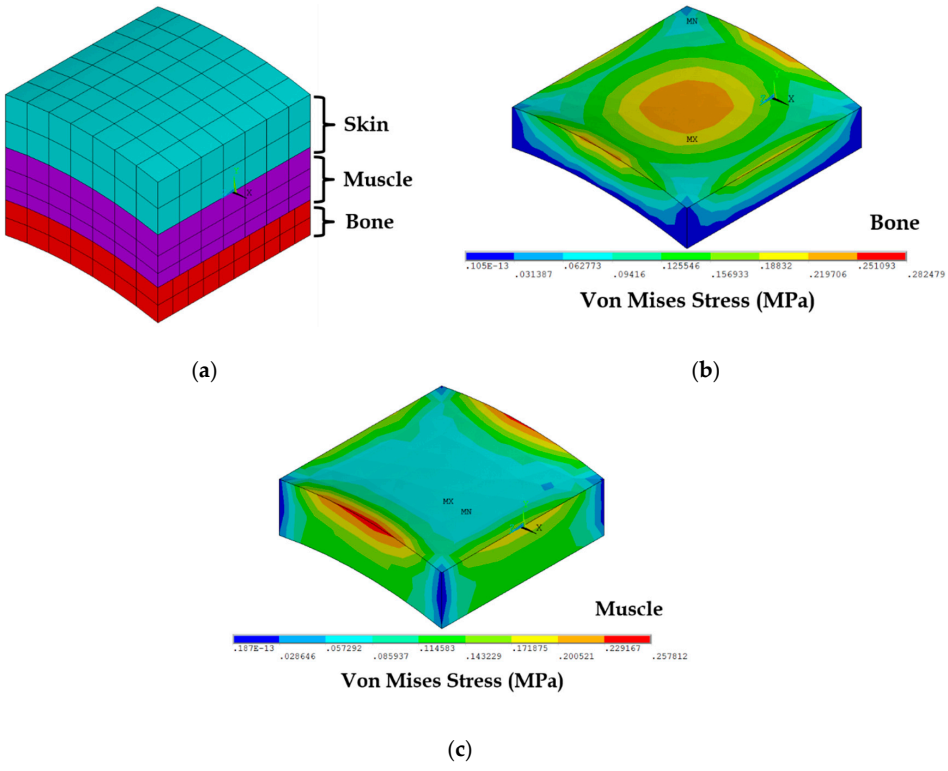

Figure 7. (**a**) Bone, muscle and skin section unprotected model (without composite coverings), Stresses generated at peak blast pressure at the (**b**) Bone section, and (**c**) Muscle section.

3.2. Blast-Induced Bone Stresses with Protective Composite Covering Variants

The resultant peak blast stresses developed at the bone section were evaluated for the six composite covering variants, namely the 0-0 short fiber type, 90-0 short fiber type, 45-45 short fiber type, 0-0 continuous fiber type, 90-0 continuous fiber type, and 45-45 continuous fiber type (presented in Figure 8). The continuous fiber based composite coverings were found to possess better blast mitigation characteristics compared to the short fiber based composite coverings. This observation is expected, as a higher degree of blast induced stress reduction is likely due to a higher volume fraction of fibers present within the continuous fiber based composite coverings. Also, there may be a slight effect of the boundary conditions selected for this study, where the continuous fibers are all constrained at both ends along the Y axis, compared to the few short fibers (which are constrained mostly at one end along the Y axis).

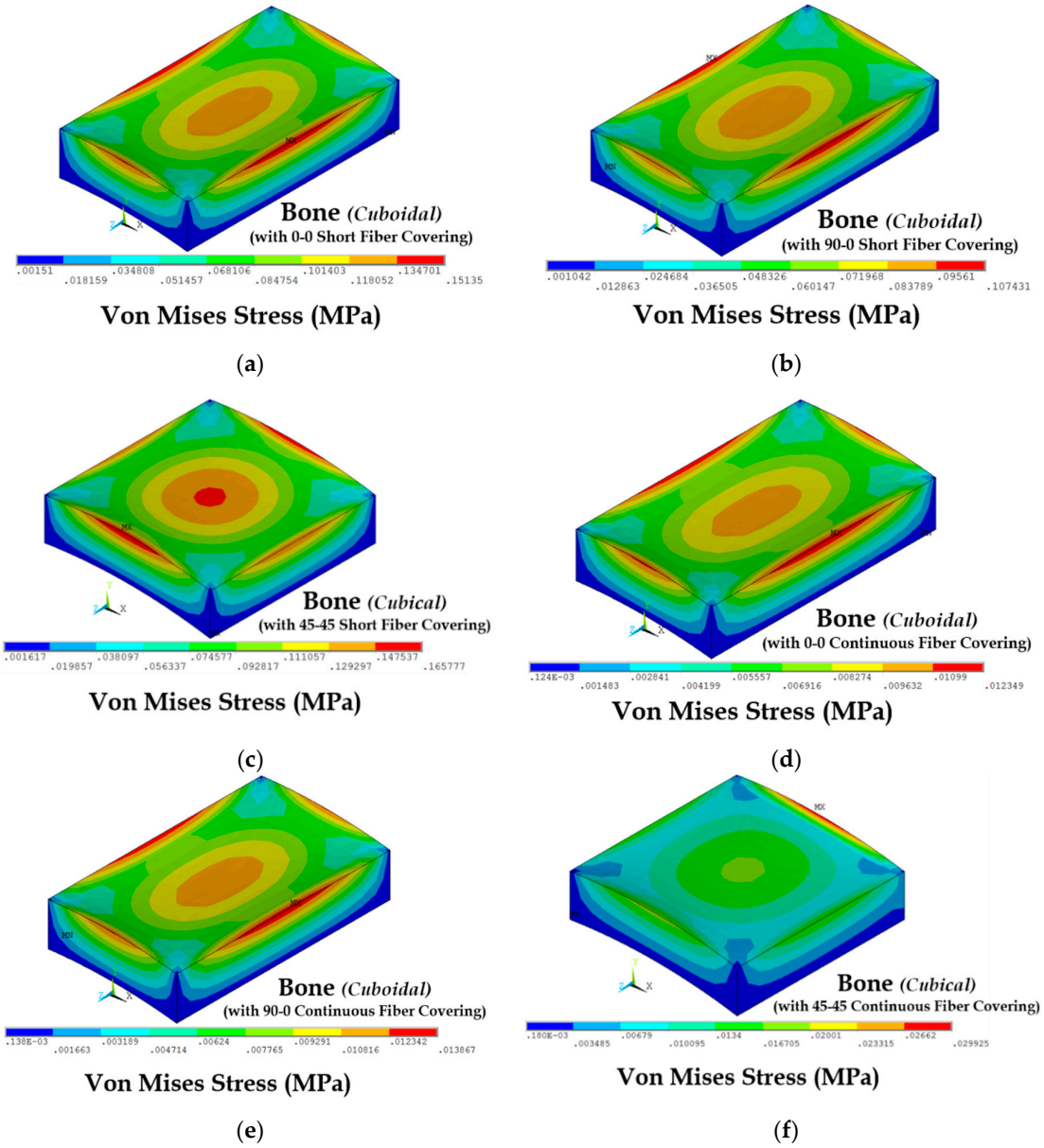

Figure 8. Resultant bone stresses due to peak blast pressure, in presence of various composite covering variants. (**a**) 0-0 short fiber; (**b**) 90-0 short fiber; (**c**) 45-45 short fiber; (**d**) 0-0 continuous fiber; (**e**) 90-0 continuous fiber; (**f**) 45-45 continuous fiber.

The induced dynamic time varying von Mises stresses at the bone section (averaged across 10 elements at the center area) generated due to the Friedlander blast loading, in presence of the different protective composite covering variants are captured in Figure 9. Among the three continuous fiber based composite coverings, the 0-0 continuous variant was found to be most effective in minimizing the resultant blast stresses at the bone section, both at the peak (seen in Figure 8) and negative blast phases. The 90-0 was found to be the second best, followed by the 45-45 orientation composite covering type for blast mitigation. This finding can be mainly explained with the differences in fiber volume fraction of each configuration, as the loading in all cases is orthogonal to the fiber directions in the composite coverings. In the 0-0 continuous variant, due to the cuboidal shape of the computational model, the length of fibers along the Z direction (0°) are longer than the fibers along the X direction (90°) in the 90-0 continuous variant. This possibly led to a slightly higher induced peak bone stresses in the 90-0 continuous variant. The shortest fiber lengths are in the 45-45 continuous variant (which is cubical in shape), which may have led to significantly higher induced peak stresses at the bone due to a low fiber volume fraction within the protective composite layers.

Among the short fiber composite cover variants, the 90-0 type led to the most significant blast mitigation, followed by the 0-0 type and 45-45 orientations. This observation is also likely due to the relative fiber volume fractions of the short fibers within the cuboidal 0-0 and 90-0 short fiber composite configurations, and the cubical 45-45 short fiber composite configuration.

The degree of average blast stress mitigation at the bone section was estimated quantitatively for the 0-0 continuous fiber-based composite covering variant, by comparing it with the unprotected model (discussed in previous section). A significant average blast stress reduction of 78% was observed with the covered model over the unprotected model. Additionally, the peak displacements were also estimated (Table 3), which exhibited a similar trend to the peak stresses.

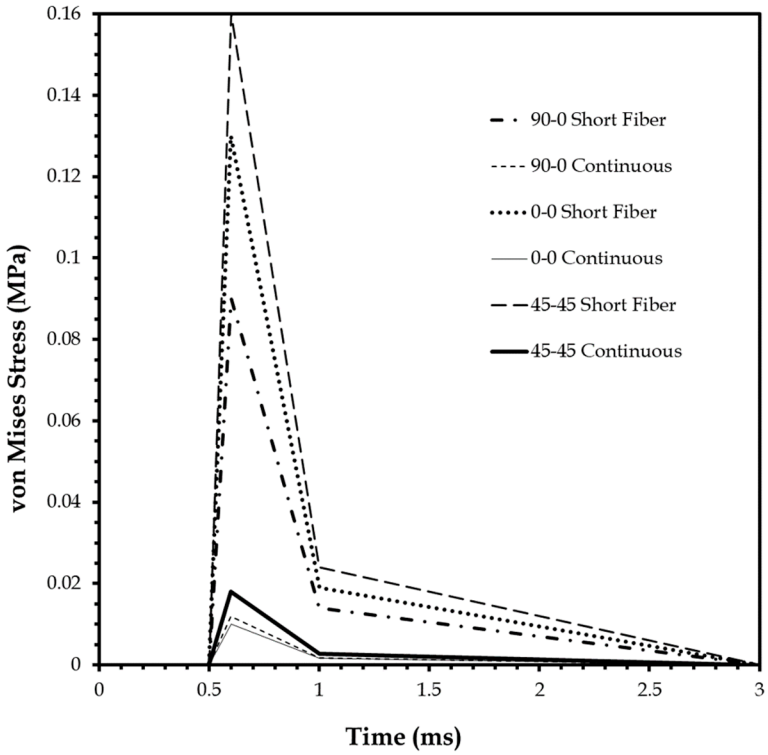

Figure 9. Comparison of the resultant dynamic bone section (averaged across 10 elements at the center area) stresses for different composite covering variants.

3.3. Blast-Induced Muscle Stresses with Composite Covering Variants

The stress field developed at the muscle section was evaluated for the peak blast pressure in presence of the different composite covering variants (Figure 10). The 0-0 continuous composite covering variant was found to cause the development of the least stresses at the center of the muscle section compared to the other composite coverings. Also, in the 0-0 continuous fiber composite layer case, the stress distribution was observed to be uniform. The specific explanation for this finding is the difference in fiber volume fraction in the composite variants, partly due to the geometrical modeling in the current work (discussed in the previous section with respect to induced bone stresses).

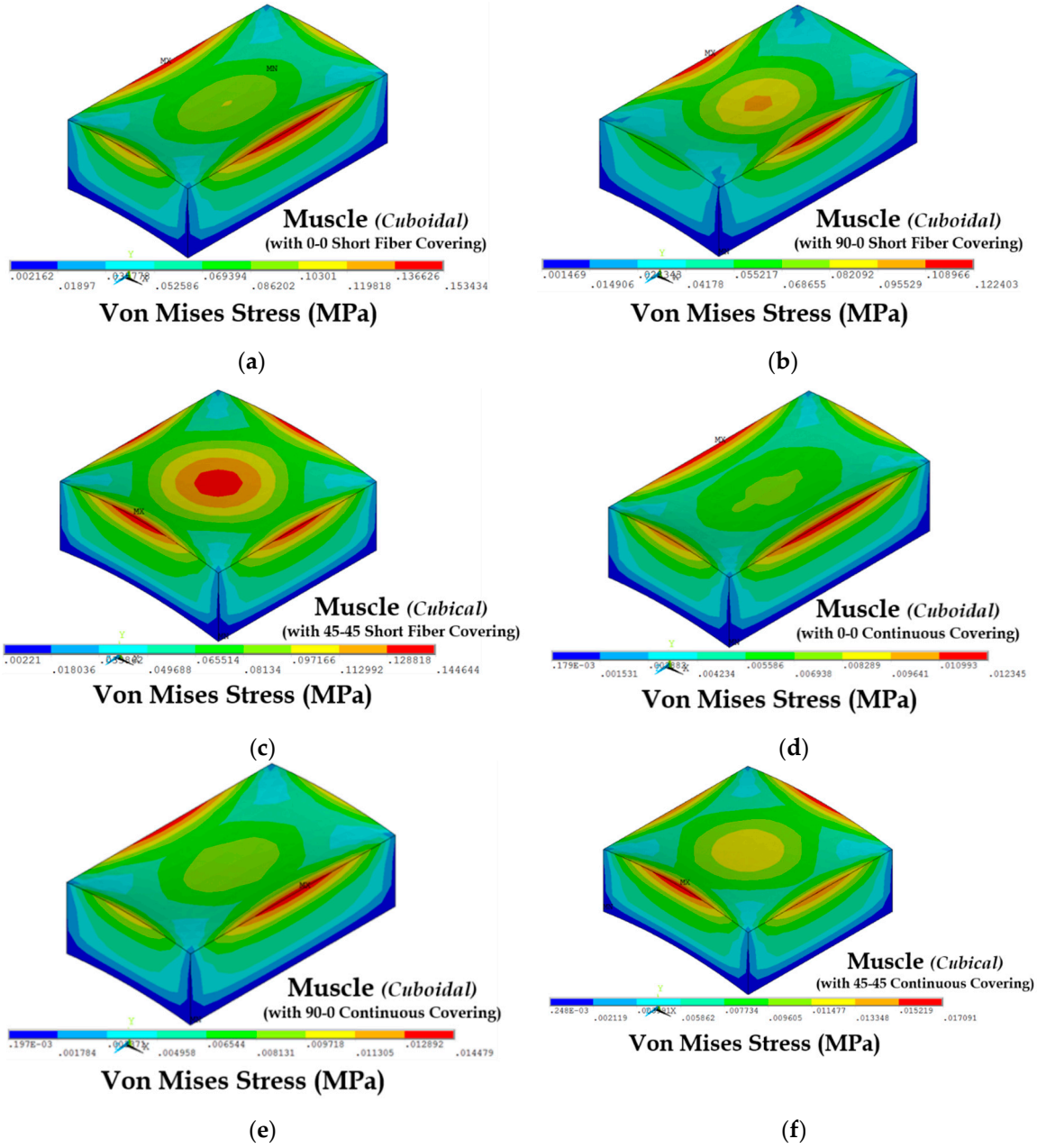

Figure 10. Resultant muscle stresses due to peak blast pressure in presence of various composite covering variants. (**a**) 0-0 short fiber; (**b**) 90-0 short fiber; (**c**) 45-45 short fiber; (**d**) 0-0 continuous fiber; (**e**) 90-0 continuous fiber; (**f**) 45-45 continuous fiber.

The resulting time varying blast-induced stresses were estimated at the muscle section for the different composite covering variants (see Figure 11). Overall, the muscle stresses were found to be lower than the bone stresses. Similar to the case of bone section, in the muscle section, the continuous composite covering types were much better in reducing the blast-induced stresses than the short fiber types. For the continuous composite covering types, the 0-0 layup had the best blast mitigation effect, followed by the 90-0 and the 45-45. These findings can be explained in a similar way to the discussion in the previous section with respect to the differences in fiber volume fractions within the computational models of the composite coverings. For the short fiber composite covering variants, the 0-0 and 90-0 lay-ups were found to cause a similar blast stress reduction at the muscle section. The reason for the similar blast reducing effect of these two variants are not clearly known. One possible explanation may be the combined effect of the fiber volume fraction differences, geometric similarities, and high cushioning effect of the muscles (compared to bones). The 45-45 short fiber lay-up case was found to most poorly absorb blast stresses (due to similar reason discussed with respect to the bones in the previous section). The percentage of average blast-induced stress reduction at the muscle section due to the 0-0 continuous composite covering case was estimated to be 70% approximately. Also, the peak muscle displacements estimated are listed in Table 3, which exhibited no outstanding trends from the peak stresses.

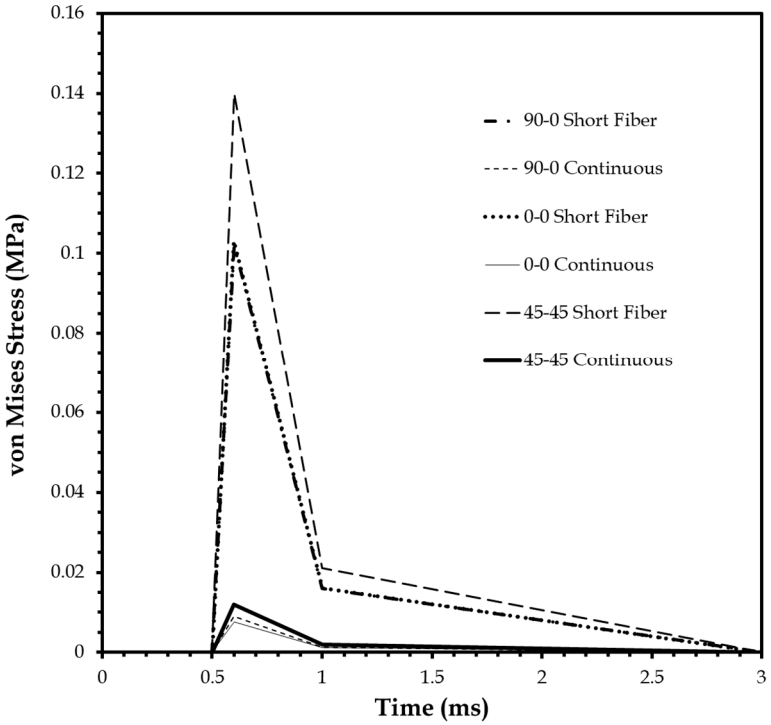

Figure 11. Comparison of the resultant dynamic muscle section (averaged across 10 elements at the center area) stresses for different composite covering variants.

Table 3. Peak bone and muscle displacements quantified for blast loading on composite coverings with different compositions.

Composite Covering	90-0 Short Fiber	90-0 Continuous	0-0 Short Fiber	0-0 Continuous	45-45 Short Fiber	45-45 Continuous
Peak Bone Displacement (10^{-5} mm)	1.22	0.16	1.73	0.13	2.13	0.24
Peak Muscle Displacement (10^{-3} mm)	3.06	0.27	3.09	0.23	4.20	0.36

3.4. Effect of Fiber Volume Fraction on Blast Absorption in 0-0 Continuous Composite Covering

The 0-0 continuous type composite covering, which was found to possess the most effective blast mitigation characteristics, was investigated further to understand the effect of varying fiber volume fraction. Three fiber volume fractions namely 0.005 (or 0.5%), 0.01 (or 10%) and 0.50 (or 50%) were simulated using pre-calculated fiber cross-sectional sizes as shown in Figure 12. Time varying blast loading was applied on the topmost surface of the protective composite covering layer.

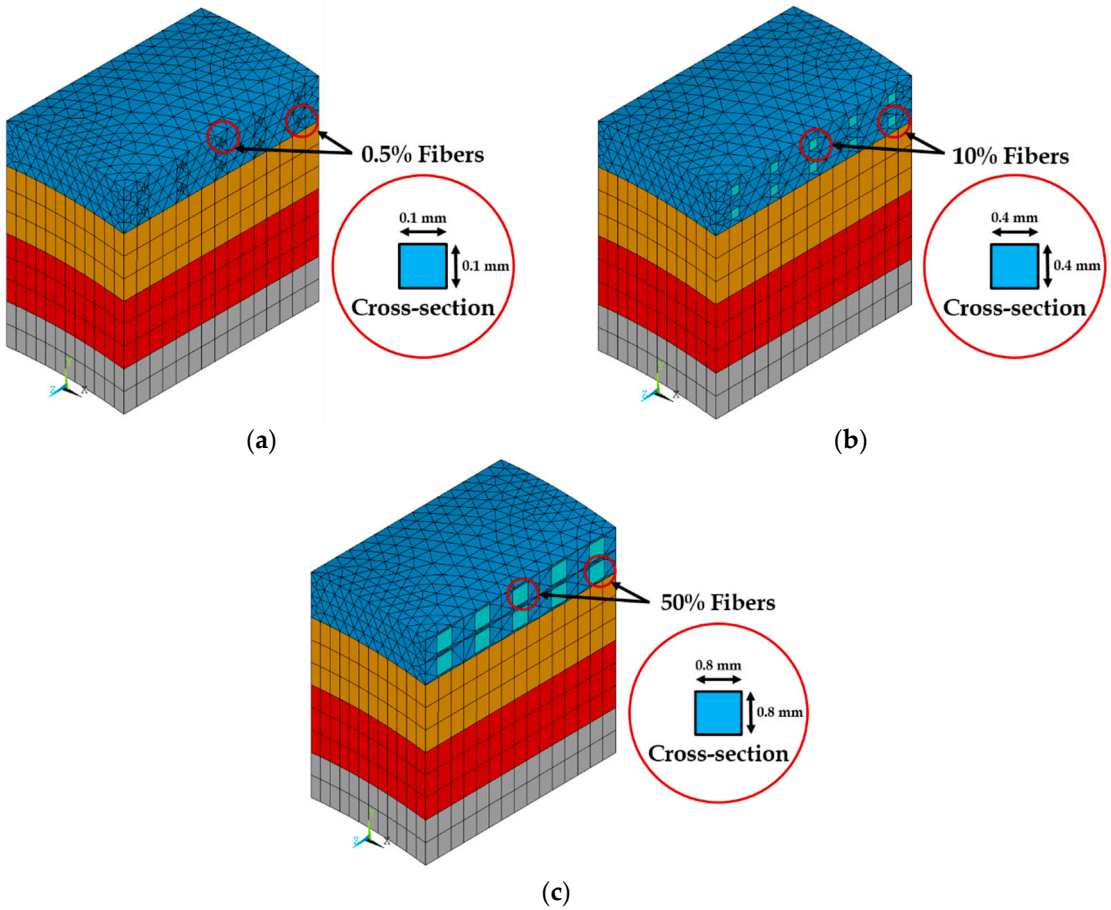

Figure 12. Three fiber volume fraction (or percentage) cases simulated for the composite layers to evaluate its effect on blast mitigation. (**a**) 0.5% fibers; (**b**) 10% fibers; (**c**) 50% fibers.

The resulting bone stresses due to the peak blast pressure were estimated numerically (Figure 13). An increase in the fiber volume fraction was found to reduce the bone stresses significantly going up from 0 to 0.5 fiber volume fraction (or 50% fibers). The stress distribution however showed a consistent

pattern. This finding not only quantifies the magnitude of the effect of fiber volume fraction variation on the induced blast stress reduction, but also validates the explanation of the differences observed in blast induced stresses with different configurations of protective composite coverings (with slightly varying fiber volume fractions).

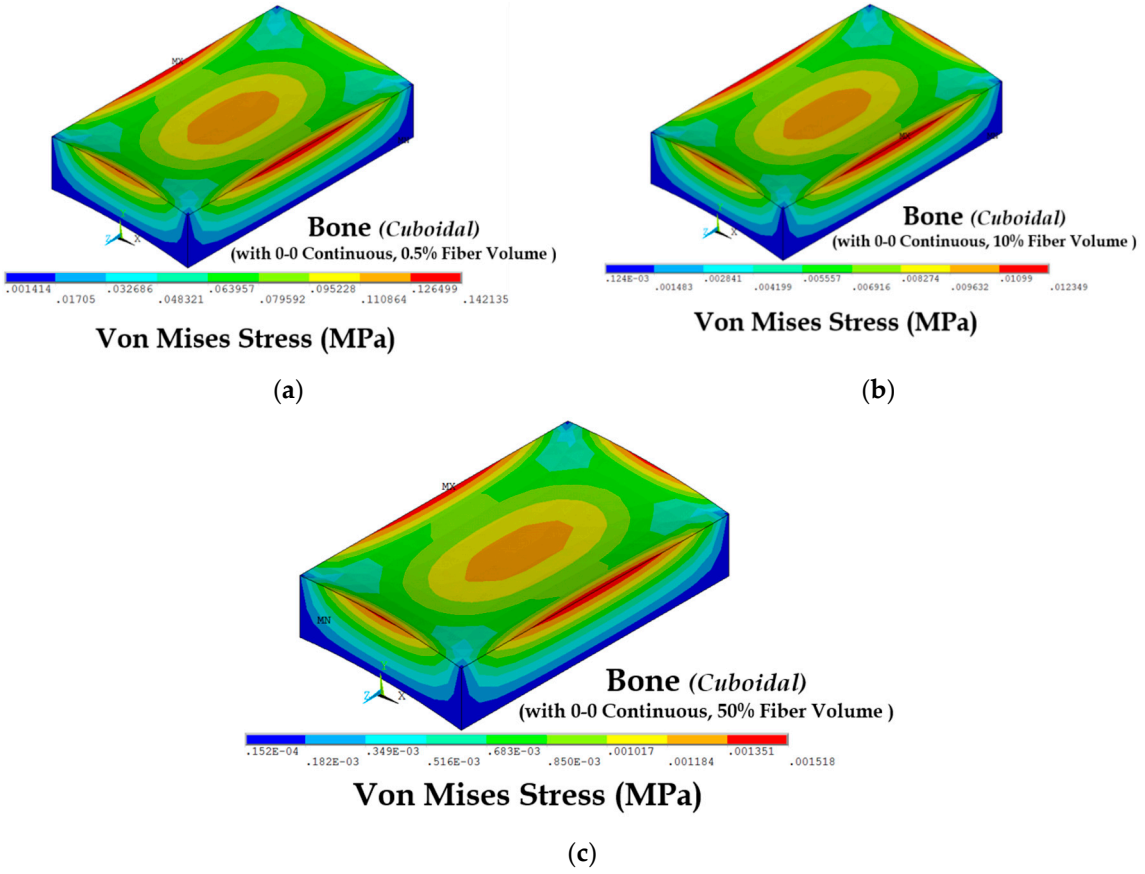

Figure 13. Bone stresses at peak blast pressure for varying fiber volume fractions (or percentages) in 0-0 continuous type composite covered numerical model. (**a**) 0.5% fibers; (**b**) 10% fibers; (**c**) 50% fibers.

Peak stresses at the bone section were quantified at the peak blast pressure, with varying fiber volume fraction for the 0-0 continuous type composite covered bone, muscle and skin model (Figure 14). A sharp drop in the bone stress was observed going from 0% fibers case to 0.5% fibers. Going from 0.5% fibers case to 10% fibers case, the drop in bone stress was less sharp than progressing from 0% fibers case to 0.5% fibers case. Further progressing from 10% to 50% fibers case, the drop in the bone stress was observed to be very gradual. It was concluded that for effective blast mitigation, a fiber volume fraction of around 0.1 (or 10%) would be optimum for an effective blast mitigation of around 78%, and 70% for the bone and muscles respectively.

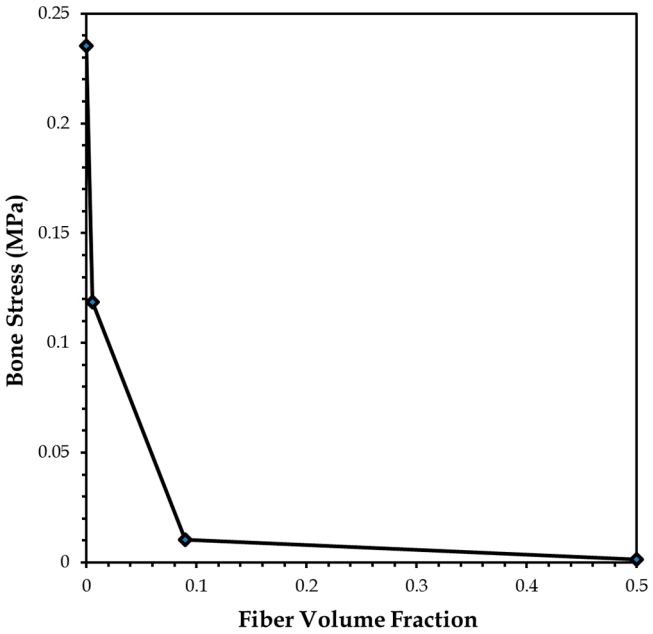

Figure 14. Bone stresses (von Mises) at peak blast pressure versus fiber volume fractions in 0-0 continuous type composite covered numerical model.

4. Conclusions

In this work, a novel elastomer-based simulant matrix material was developed, which is flexible and can be casted in any shape or size. This material was embedded numerically with Kevlar 129 material (which is known for its good impact resistance in the field of ballistics) to simulate protective composite coverings. The resulting composite covering layers were modeled numerically to protect a bone, muscle and skin section model of the human body against blast loads. The effect of varying fiber orientation, fiber length, and fiber volume fraction on the blast mitigation effectiveness of the composite covering layer were studied (in terms of reduction in induced blast stress at the bone and muscle layers). From the analyses, it was found that the 0-0 continuous fiber configuration with a fiber volume fraction close to 0.1 was most effective in reducing blast-induced stresses at the bone and muscle sections. The key contributing factor for the effectiveness of this composite variant to mitigate blast induced stresses was observed to be the optimal fiber volume fraction. To date, such a skin-like composite material (composed of Kevlar fibers embedded within a skin simulant) has not been developed for evaluation of blast resistance, which could be useful in designing and manufacturing of whole body composite armor reinforcements for mitigating blast injury and trauma in the future. A major limitation of this study is the lack of experimental validation due to lack of resources, which should be a subject of future studies to confirm the blast mitigation efficiency of the modeled composite covering. Also, increasing the composite layer thickness from 2 mm to approximately 10 mm may further improve the effectivity of blast resistance of the tested composite covering material. Additionally, it should be noted that the results from this analysis are limited to the boundary conditions selected for this study. Specifically, if the constraints at the edges of the studied unit cell were modified to be deformable in all directions, the induced stress distributions may significantly change, with slight effect on the peak stresses. Incorporating a more realistic set of boundary conditions will be the subject of future studies.

Author Contributions: Conceptualization, A.C.; Data curation, R.G.; Formal analysis, R.G.; Supervision, A.C.; Writing—original draft, A.C.

Funding: This research received no external funding.

Acknowledgments: A.C. would like to acknowledge the collaboration with the Advanced Computational and Experimental Mechanics Lab (ACEML) at the University of Alabama for assistance with experimental testing.

Conflicts of Interest: The authors declare no conflict of interest.

References

1. Schneiderman, A.I.; Braver, E.R.; Kang, H.K. Understanding sequelae of injury mechanisms and mild traumatic brain injury incurred during the conflicts in iraq and afghanistan: Persistent postconcussive symptoms and posttraumatic stress disorder. *Am. J. Epidemiol.* **2008**, *167*, 1446–1452. [CrossRef] [PubMed]
2. Kulkarni, S.; Gao, X.-L.; Horner, S.; Zheng, J.; David, N. Ballistic helmets–their design, materials, and performance against traumatic brain injury. *Compos. Struct.* **2013**, *101*, 313–331. [CrossRef]
3. Carey, M.E.; Herz, M.; Corner, B.; McEntire, J.; Malabarba, D.; Paquette, S.; Sampson, J.B. Ballistic helmets and aspects of their design. *Neurosurgery* **2000**, *47*, 678–689. [PubMed]
4. Khalil, T.B.; Goldsmith, W.; Sackman, J. Impact on a model head-helmet system. *Int. J. Mech. Sci.* **1974**, *16*, 609–625. [CrossRef]
5. Van Hoof, J. *Modelling of Impact Induced Delamination in Composite Materials*; Carleton University: Ottawa, ON, Canada, 1999.
6. Van Hoof, J.; Worswick, M. *Combining Head Models with Composite Models to Simulate Ballistic Impacts*; Waterloo Univ (Ontario) Dept of Mechanical Engineering: Waterloo, ON, Canada, 2001.
7. Daniel, B.; Rémy, W. Finite element modelling of human head injuries caused by ballistic projectiles. *Revue Européenne des Eléments* **2005**, *14*, 559–576. [CrossRef]
8. Aare, M.; Kleiven, S. Evaluation of head response to ballistic helmet impacts using the finite element method. *Int. J. Impact Eng.* **2007**, *34*, 596–608. [CrossRef]
9. Lee, H.-P.; Gong, S. Finite element analysis for the evaluation of protective functions of helmets against ballistic impact. *Comput. Methods Biomech. Biomed. Eng.* **2010**, *13*, 537–550. [CrossRef] [PubMed]
10. Tan, L.B.; Tse, K.M.; Lee, H.P.; Tan, V.B.C.; Lim, S.P. Performance of an advanced combat helmet with different interior cushioning systems in ballistic impact: Experiments and finite element simulations. *Int. J. Impact Eng.* **2012**, *50*, 99–112. [CrossRef]
11. Li, Y.; Li, X.; Gao, X.-L. Modeling of advanced combat helmet under ballistic impact. *J. Appl. Mech.* **2015**, *82*, 111004. [CrossRef]
12. Rodríguez-Millán, M.; Ito, T.; Loya, J.; Olmedo, A.; Miguélez, M. Development of numerical model for ballistic resistance evaluation of combat helmet and experimental validation. *Mater. Des.* **2016**, *110*, 391–403. [CrossRef]
13. Sarvghad-Moghaddam, H.; Karami, G.; Ziejewski, M. The effects of directionality of blunt impacts on mechanical response of the brain. In Proceedings of the ASME 2014 International Mechanical Engineering Congress and Exposition, Montreal, QC, Canada, 14–20 November 2014; p. V003T003A013.
14. Ganpule, S.; Gu, L.; Alai, A.; Chandra, N. Role of helmet in the mechanics of shock wave propagation under blast loading conditions. *Comput. Methods Biomech. Biomed. Eng.* **2012**, *15*, 1233–1244. [CrossRef] [PubMed]
15. Moss, W.C.; King, M.J.; Blackman, E.G. Skull flexure from blast waves: A mechanism for brain injury with implications for helmet design. *Phys. Rev. Lett.* **2009**, *103*, 108702. [CrossRef] [PubMed]
16. Zhang, T.G.; Satapathy, S.S.; Dagro, A.M.; McKee, P.J. Numerical study of head/helmet interaction due to blast loading. In Proceedings of the ASME 2013 International Mechanical Engineering Congress and Exposition, San Diego, CA, USA, 15–21 November 2013; p. V03AT03A004.
17. Nyein, M.K.; Jason, A.M.; Yu, L.; Pita, C.M.; Joannopoulos, J.D.; Moore, D.F.; Radovitzky, R.A. In silico investigation of intracranial blast mitigation with relevance to military traumatic brain injury. *Proc. Natl. Acad. Sci. USA* **2010**. [CrossRef] [PubMed]
18. Sarvghad-Moghaddam, H.; Rezaei, A.; Ziejewski, M.; Karami, G. Evaluation of brain tissue responses because of the underwash overpressure of helmet and faceshield under blast loading. *Int. J. Numer. Methods Biomed. Eng.* **2017**, *33*, e02782. [CrossRef] [PubMed]
19. Sarvghad-Moghaddam, H.; Jazi, M.S.; Rezaei, A.; Karami, G.; Ziejewski, M. Examination of the protective roles of helmet/faceshield and directionality for human head under blast waves. *Comput. Methods Biomech. Biomed. Eng.* **2015**, *18*, 1846–1855. [CrossRef] [PubMed]

20. Sarvghad-Moghaddam, H.; Rezaei, A.; Ziejewski, M.; Karami, G. Correlative analysis of head kinematics and brain's tissue response: A computational approach toward understanding the mechanisms of blast tbi. *Shock Waves* **2017**, *27*, 919–927. [CrossRef]
21. Chanda, A.; Unnikrishnan, V. Effect of bladder and rectal loads on the vaginal canal and levator ani in varying pelvic floor conditions. *Mech. Adv. Mater. Struct.* **2017**. [CrossRef]
22. Rodríguez-Millán, M.; Tan, L.; Tse, K.; Lee, H.; Miguelez, M. Effect of full helmet systems on human head responses under blast loading. *Mater. Des.* **2017**, *117*, 58–71. [CrossRef]
23. Grujicic, M.; Bell, W.; Pandurangan, B.; He, T. Blast-wave impact-mitigation capability of polyurea when used as helmet suspension-pad material. *Mater. Des.* **2010**, *31*, 4050–4065. [CrossRef]
24. Grujicic, M.; Pandurangan, B.; Bell, W.; Bagheri, S. Shock-wave attenuation and energy-dissipation potential of granular materials. *J. Mater. Eng. Perform.* **2012**, *21*, 167–179. [CrossRef]
25. Jenson, D.; Unnikrishnan, V. Multiscale simulation of ballistic composites for blast induced traumatic brain injury mitigation. In Proceedings of the ASME 2014 International Mechanical Engineering Congress and Exposition, Montreal, QC, Canada, 14–20 November 2014; p. V009T012A072.
26. Jenson, D.; Unnikrishnan, V.U. Energy dissipation of nanocomposite based helmets for blast-induced traumatic brain injury mitigation. *Compos. Struct.* **2015**, *121*, 211–216. [CrossRef]
27. Chanda, A.; Callaway, C. Computational modeling of blast induced whole-body injury: A review. *J. Med. Eng. Technol.* **2018**, *42*, 88–104. [CrossRef] [PubMed]
28. Chanda, A.; Unnikrishnan, V. Subject-specific computational study of blast induced traumatic injuries. In Proceedings of the Society of Engineering Science 52nd Annual Technical Meeting, College Station, TX, USA, 26–28 October 2015.
29. Chanda, A.; Callaway, C.; Clifton, C.; Unnikrishnan, V. *Biofidelic Human Brain Tissue Surrogates*; Taylor & Francis: Oxfordshire, UK, 2016.
30. Chanda, A.; Unnikrishnan, V. Human tissue simulants for study of traumatic brain injury (tbi). In Proceedings of the American Society for Composites: Thirty-First Technical Conference, Williamsburg, VA, USA, 19–22 September 2016.
31. Chanda, A.; Unnikrishnan, V. A realistic 3d computational model of the closure of skin wound with interrupted sutures. *J. Mech. Med. Biol.* **2017**, *17*, 1750025. [CrossRef]
32. Chanda, A.; Curry, K. Patient-specific biofidelic human coronary artery surrogates. *J. Mech. Med. Biol.* **2018**, *18*. [CrossRef]
33. Gray, H.; Goss, C.M.; Alvarado, D.M. *Anatomy of the Human Body*; Lea & Febiger: Philadelphia, PA, USA, 1973.
34. Chanda, A.; Graeter, R.; Unnikrishnan, V. Effect of blasts on subject-specific computational models of skin and bone sections at various locations on the human body. *AIMS Mater. Sci.* **2015**, *2*, 425–447. [CrossRef]
35. Annaidh, A.N.; Bruyère, K.; Destrade, M.; Gilchrist, M.D.; Otténio, M. Characterization of the anisotropic mechanical properties of excised human skin. *J. Mech. Behav. Biomed. Mater.* **2012**, *5*, 139–148. [CrossRef] [PubMed]
36. Chanda, A.; Unnikrishnan, V. Customized Insoles for Diabetic and Pressure Ulcers. U.S. Patent 15/646,046, 11 January 2018.
37. Shergold, O.A.; Fleck, N.A.; Radford, D. The uniaxial stress versus strain response of pig skin and silicone rubber at low and high strain rates. *Int. J. Impact Eng.* **2006**, *32*, 1384–1402. [CrossRef]
38. Martins, P.; Natal Jorge, R.; Ferreira, A. A comparative study of several material models for prediction of hyperelastic properties: Application to silicone-rubber and soft tissues. *Strain* **2006**, *42*, 135–147. [CrossRef]
39. Chanda, A.; Unnikrishnan, V.; Roy, S.; Richter, H.E. Computational modeling of the female pelvic support structures and organs to understand the mechanism of pelvic organ prolapse: A review. *Appl. Mech. Rev.* **2015**, *67*, 040801. [CrossRef]
40. Chanda, A.; Meyer, I.; Richter, H.E.; Lockhart, M.E.; Moraes, F.R.; Unnikrishnan, V. Vaginal changes due to varying degrees of rectocele prolapse: A computational study. *J. Biomech. Eng.* **2017**, *139*, 101001. [CrossRef] [PubMed]
41. Chanda, A.; Unnikrishnan, V.; Richter, H.E.; Lockhart, M.E. Computational modeling of anterior and posterior pelvic organ prolapse (pop). In Proceedings of the ASME 2016 International Mechanical Engineering Congress and Exposition, Phoenix, AZ, USA, 11–17 November 2016; p. V009T012A085.
42. Gonzalez, L.Y.S.; Botero, M.G.; Betancur, M. *Hyperelastic Material Modeling*; Technical Report; Departamento de Ingenieria Mecanica, Universidad EAFIT: Medellın, Colombia, 2005.

43. Holzapfel, G.A. *Nonlinear Solid Mechanics*; Wiley: Chichester, UK, 2000; Volume 24.
44. Chanda, A.; Unnikrishnan, V.; Richter, H.E.; Lockhart, M.E. A biofidelic computational model of the female pelvic system to understand effect of bladder fill and progressive vaginal tissue stiffening due to prolapse on anterior vaginal wall. *Int. J. Numer. Methods Biomed. Eng.* **2016**, *32*, e02767. [CrossRef] [PubMed]
45. Chanda, A.; Flynn, Z.; Unnikrishnan, V. Biomechanical characterization of normal and prolapsed vaginal tissue surrogates. *J. Mech. Med. Biol.* **2018**, *18*, 1750100. [CrossRef]
46. Chanda, A.; Callaway, C. Tissue anisotropy modeling using soft composite materials. *Appl. Bionics Biomech.* **2018**, *2018*, 4838157. [CrossRef] [PubMed]
47. Chanda, A.; Unnikrishnan, V.; Lackey, K. Biofidelic conductive synthetic skin composites. In Proceedings of the American Society for Composites—Thirty-Second Technical Conference, West Lafayette, IN, USA, 23–25 October 2017.
48. Chanda, A. *Biofidelic Soft Composites–Experimental and Computational Modeling*; University of Alabama Libraries: Tuscaloosa, AL, USA, 2017.
49. Lim, J.; Chen, W.W.; Zheng, J.Q. Dynamic small strain measurements of kevlar® 129 single fibers with a miniaturized tension kolsky bar. *Polymer Test.* **2010**, *29*, 701–705. [CrossRef]
50. Zhu, D.; Mobasher, B.; Rajan, S.D. Dynamic tensile testing of kevlar 49 fabrics. *J. Mater. Civ. Eng.* **2010**, *23*, 230–239. [CrossRef]
51. Bertucci, R.; Liao, J.; Williams, L. Development of a lower extremity model for finite element analysis at blast condition. In Proceedings of the ASME 2011 Summer Bioengineering Conference, Farmington, PA, USA, 22–25 June 2011; pp. 1035–1036.
52. Flynn, C.O. *The Design and Validation of a Multi-Layer Model of Human Skin*; Institute of Technology: Sligo, Ireland, 2007.
53. Chanda, A.; Ruchti, T.; Unnikrishnan, V. Computational modeling of wound suture: A review. *IEEE Rev. Biomed. Eng.* **2018**. [CrossRef] [PubMed]
54. Chanda, A.; Unnikrishnan, V.; Flynn, Z.; Lackey, K. Experimental study on tissue phantoms to understand the effect of injury and suturing on human skin mechanical properties. *Proc. Inst. Mech. Eng. Part H J. Eng. Med.* **2017**, *231*, 80–91. [CrossRef] [PubMed]
55. Chanda, A.; Unnikrishnan, V.; Flynn, Z. Biofidelic Human Skin Simulant. U.S. Patent 15/204353, 7 July 2015.
56. Chanda, A.; Flynn, Z.; Unnikrishnan, V. Biofidelic Vaginal Tissue Surrogate. US Provisional Patent No. 62/263942, 7 July 2015.
57. Jones, R.M. *Mechanics of Composite Materials*; McGraw-Hill: New York, NY, USA, 1975; Volume 1.
58. McGrath, J.; Uitto, J. Anatomy and organization of human skin. In *Rook's Textbook of Dermatology*, 8th ed.; Blackwell Science Ltd: Oxford, UK, 2010; pp. 1–53.
59. Abe, T.; DeHoyos, D.V.; Pollock, M.L.; Garzarella, L. Time course for strength and muscle thickness changes following upper and lower body resistance training in men and women. *Eur. J. Appl. Physiol.* **2000**, *81*, 174–180. [CrossRef] [PubMed]
60. De Boer, M.D.; Seynnes, O.R.; Di Prampero, P.E.; Pišot, R.; Mekjavić, I.B.; Biolo, G.; Narici, M.V. Effect of 5 weeks horizontal bed rest on human muscle thickness and architecture of weight bearing and non-weight bearing muscles. *Eur. J. Appl. Physiol.* **2008**, *104*, 401–407. [CrossRef] [PubMed]
61. Durnin, J.; Rahaman, M. The assessment of the amount of fat in the human body from measurements of skinfold thickness. *Br. J. Nutr.* **1967**, *21*, 681–689. [CrossRef] [PubMed]
62. Tucker, C.L., III; Liang, E. Stiffness predictions for unidirectional short-fiber composites: Review and evaluation. *Compos. Sci. Technol.* **1999**, *59*, 655–671. [CrossRef]
63. Ghoneim, H.; Chanda, A. Pumping potential of a left-ventricle-like flexiblematrix-composite structure. In Proceedings of the 19th international conference on composite materials (ICCM19), Montreal, QC, Canada, 28 July–2 August 2013; pp. 7457–7462.
64. Chanda, A.; Ghoneim, H. Pumping potential of a two-layer left-ventricle-like flexible-matrix-composite structure. *Compos. Struct.* **2015**, *122*, 570–575. [CrossRef]
65. Chanda, A.; Unnikrishnan, V.; Flynn, Z. Biofidelic Skin Simulant. U.S. Patent US20170011657A1, 12 January 2017.
66. Wang, E.; Nelson, T.; Rauch, R. Back to elements-tetrahedra vs. Hexahedra. In Proceedings of the 2004 International ANSYS Conference, Canonsburg, PA, USA, 24–26 May 2004.

67. Singleton, J.; Gibb, I.; Bull, A.; Clasper, J. Traumatic amputation from explosive blast: Evidence for a new injury mechanism. In *Orthopaedic Proceedings*; The British Editorial Society of Bone & Joint Surgery: London, UK, 2013; Volume 95, p. 2.
68. Webster, C.; Masouros, S.; Gibb, I.; Clasper, J. Fracture patterns in pelvic blast injury: A retrospective analysis and implications for future preventative strategies. In *Orthopaedic Proceedings*; The British Editorial Society of Bone & Joint Surgery: London, UK, 2015; Volume 97, p. 14.
69. Sheean, A.J.; Tintle, S.M.; Rhee, P.C. Soft tissue and wound management of blast injuries. *Curr. Rev. Musculoskelet. Med.* **2015**, *8*, 265–271. [CrossRef] [PubMed]